

A Tight Relation between Spiral Arm Pitch Angle and Protoplanetary Disk Mass

SI-YUE YU,^{1,2} LUIS C. HO,^{1,2} AND ZHAOHUAN ZHU³

¹*Kavli Institute for Astronomy and Astrophysics, Peking University, Beijing 100871, China*

²*Department of Astronomy, School of Physics, Peking University, Beijing 100871, China*

³*Department of Physics and Astronomy, University of Nevada, Las Vegas, 4505 South Maryland Parkway, Las Vegas, NV 89154, USA*

ABSTRACT

We use two-dimensional Fourier transformation to measure the pitch angle (φ) of the dominant spiral Fourier mode of well-defined spiral arms in 13 protoplanetary disks, making use of near-infrared scattered-light images of AB Aur, SAO 206462, MWC 758, V1247 Ori, HD 142527, DZ Cha, LkH α 330, and HD 100453, and ALMA millimeter continuum images of Elias 2-27, IM Lup, AS 205, and HT Lup. We find that the measured pitch angle correlates strongly with disk mass (M_D), such that more massive protoplanetary disks have smaller pitch angles, following $|\varphi| = -(7.8 \pm 1.7) \log(M_D/M_\odot) + (2.7 \pm 2.6)$. Interestingly, four disks with a known companion (HD 142527, HD 100453, AS 205, and HT Lup) share the same trend. Such a strong dependence of spiral arm pitch angle on disk mass suggests that the disk mass, independent of the formation mechanism, plays a fundamental role in determining the arm tightness of the observed spiral structure. The physical origin of the $\varphi - M_D$ relation is still not clear. The pitch angle of spiral arms in protoplanetary disks provides an independent constraint on the disk mass.

Keywords: circumstellar matter — protoplanetary disks: spiral — protoplanetary disks: structure — stars: protostars

1. INTRODUCTION

Well-defined spiral structure has been detected in protoplanetary disks owing to high-spatial resolution observations, in both near-infrared (NIR) scattered-light images of AB Aur (Hashimoto et al. 2011), SAO 206462 (Muto et al. 2012; Garufi et al. 2013), MWC 758 (Grady et al. 2013; Benisty et al. 2015), V1247 Ori (Ohta et al. 2016), HD 142527 (Avenhaus et al. 2017), HD 100453 (Wagner et al. 2015; Benisty et al. 2017), DZ Cha (Canovas et al. 2018), and LkH α 330 (Uyama et al. 2018), and in Atacama Large Millimeter/submillimeter Array (ALMA) millimeter continuum images of Elias 2-27 (Pérez et al. 2016; Huang et al. 2018), IM Lup (Huang et al. 2018), WaOph 6 (Huang et al. 2018), AS 205 (Kurtovic et al. 2018), and HT Lup (Kurtovic et al. 2018). Spiral arms in HD 100546 exhibit different chirality (Follette et al. 2017) and thus are not well-defined. Because of the large dust scattering opacity, NIR scattered-light observations detect structure on the disk surface, while ALMA millimeter continuum observations probe the cold dust in the disk midplane. The spirals of MWC 758 coexist both in the NIR and millimeter continuum images (Boehler et al. 2018; Dong et al. 2018a), but the latter are much more asymmetric. Most of the disks with spi-

ral arms observed in the NIR show a peculiar dip in the infrared spectral energy distribution that may indicate a lack of warm dust near the central star (Strom et al. 1989; Skrutskie et al. 1990; Garufi et al. 2018), suggesting that the mechanism to form gaps may be related to spiral arm formation. These results, however, may be affected by small sample size or observational selection effects.

Pitch angle (φ), defined as the angle between the tangent of a spiral arm and the azimuthal direction, describes the degree of tightness of the arm. The classic quasi-stationary density wave theory, proposed by Lin & Shu (1964), is perhaps the most successful framework to explain spiral structure in galaxies. In this framework, a number of works aimed to understand linear nonaxisymmetric density perturbations, including dipole or spiral perturbations, in gaseous and collisionless self-gravitating disks (Adams et al. 1989; Shu et al. 1990; Noh et al. 1991; Laughlin & Rozyczka 1996). However, these linear stability analyses have not investigated the pitch angle of spiral arms in the disks. In contrast, Rafikov (2002) studied the nonlinear propagation of a one-armed spiral wake launched by a planet embedded in a disk. Using weakly nonlinear density wave theory in the WKB limit, Rafikov proposed that

the pitch angle of planet-generated spiral arms depends on the sound speed of the disk and the location of the planet. Muto et al. (2012) and Benisty et al. (2015) applied this scenario to SAO 206462 and MWC 758, respectively, to infer the properties of their protoplanetary disks and the position of the hypothetical unseen planet. The recent studies of Bae & Zhu (2018) and Miranda & Rafikov (2019) further show, based on linear theory, that in addition to this main arm, a secondary arm can arise in the inner part of the disk. Similarly, in hydrodynamical simulations the presence of a massive companion can induce spiral arms (e.g. Kley & Nelson 2012; Zhu et al. 2015) that well match observations (Dong et al. 2015a, 2016). Zhu et al. (2015), in particular, showed that, in addition to the sound speed in the disk and the location of the perturber, the pitch angle of planet-induced spiral arms also depends on the mass of the planet, such that arms become more open with a more massive perturber.

Gravitational instability, often explored using simulations (e.g., Lodato & Rice 2004; Rice et al. 2004; Forgan et al. 2011), is another possible mechanism to generate spiral arms in circumstellar disks. One apparent shortcoming of these simulations is that they tend to produce a significantly larger number of arms than the two normally observed. Recent studies show that such simulations of gravitationally unstable disks are also able to generate two-armed spirals (Dong et al. 2015b; Tomida et al. 2017), which qualitatively match the observed arms in the Elias 2-27 disk (Meru et al. 2017; Tomida et al. 2017). But these simulated spirals disappear in a few rotations (Tomida et al. 2017), implying that their shape and, hence, the pitch angle of the simulated spirals also change frequently with time.

Pressure variations due to shadowing from a misaligned inner disk have been proposed to trigger spiral arms observed in scattered light (Montesinos et al. 2016; Montesinos & Cuello 2018). As the simulations of Montesinos et al. (2016) show, a less massive disk may have more open arms, which, however, would eventually evolved into tight arms.

Note that these mechanisms of spiral arm formation are not necessarily mutually exclusive. For example, a tidal interaction theoretically can induce an external perturbation, which results in spiral structure obeying density wave theory, with, perhaps, gravitational instability participating in it, making the structure more complicated.

The pitch angle of spiral arms may shed light on their formation mechanism. We aim to establish the dependence of pitch angle on the properties of protoplanetary disks to probe the physical origin of spiral arms.

2. DATA

This study makes use of the following data:

VLT/SPHERE images of MWC 758 (Benisty et al. 2015), HD 142527 (Avenhaus et al. 2017), DZ Cha (Canovas et al. 2018), and HD 100453 (Benisty et al. 2017); VLT/NACO image of SAO 206462 (Garufi et al. 2013); Subaru/HiCIAO images of AB Aur (Hashimoto et al. 2011), LkH α 330 (Uyama et al. 2018), and V1247 Ori (Ohta et al. 2016), and ALMA millimeter continuum images of Elias 2-27, IM Lup, WaOph 6, AS 205, and HT Lup from the Disk Substructures at High Angular Resolution Project (DSHARP) (Andrews et al. 2018; Huang et al. 2018; Kurtovic et al. 2018).

With the exception of Elias 2-27, WaOph 6, AS 205, and HT Lup, the masses of the protoplanetary disks (M_D) are from Dong et al. (2018b), who converted the dust submillimeter continuum emission at 880 μm to total mass assuming a dust opacity of $\kappa = 3 \text{ cm}^2 \text{ g}^{-1}$ and a gas-to-dust mass ratio of 100. We compute M_D for Elias 2-27, WaOph 6, AS 205, and HT Lup following the procedure described in Dong et al. (2018b), adopting the disk radius in our Table 1 and spectral energy distributions (SED) and other parameters collected by Andrews et al. (2018). The uncertainties of the disk masses are estimated by assigning fractional errors of 15%, 15%, and 30% to the submillimeter fluxes, dust opacity, and gas-to-dust mass ratio, respectively.

To roughly estimate Toomre's (1964) Q of the disk, we assume a Keplerian disk heated by the irradiation of a central star. The dust temperature follows $T = \{\phi L_*/8\pi\sigma_{\text{SB}}r^2\}^{1/4}$, where ϕ , set to 0.02 for simplicity, is the flaring angle, L_* is the luminosity of the central star, and σ_{SB} is the Stefan-Boltzmann constant. Then we have sound speed $c_s = \sqrt{k_{\text{B}}T/2.3m_p}$, with the Boltzmann constant k_{B} and proton mass m_p . The mean surface density is estimated as $\bar{\Sigma} = M_D/\pi R_D^2$, for disk radius R_D . The mean Q is derived as $Q = c_s\kappa/\pi G\bar{\Sigma}$, where c_s and epicyclic frequency κ are estimated at $r = R_D$. The disk aspect ratio H/R , with $H \equiv c_s/\Omega$ and Ω the angular velocity, is evaluated at $r = R_D$.

Table 1 lists the parameters for the protoplanetary disks and their central stars used in this work: inclination angle (i), position angle (PA), disk radius (R_D), mass of central star (M_*), flux density at 880 μm ($f_{880\mu\text{m}}$), disk mass (M_D), luminosity of central star (L_*), mean Toomre's Q , disk aspect ratio (H/R), and pitch angle (φ).

3. MEASUREMENT OF PITCH ANGLE

For the NIR scattered-light images, we scale each pixel with the square of its distance from the star (r^2) to compensate for the r^{-2} dependence of the stellar illumina-

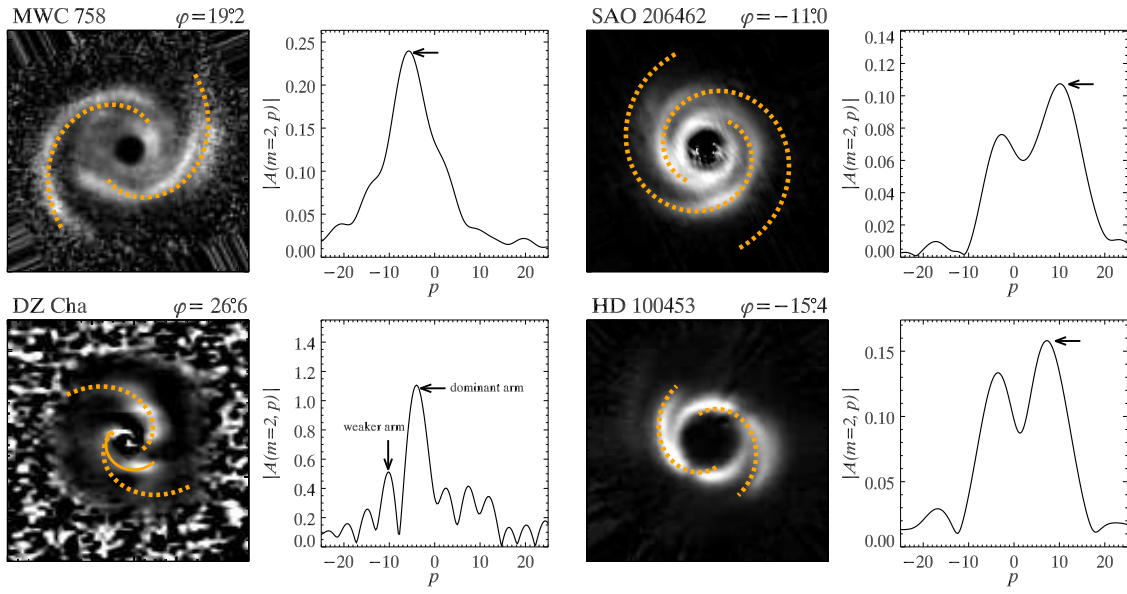


Figure 1. Illustration of pitch angle measurement for MWC 758, SAO 206462, DZ Cha, and HD 100453. (Left) Deprojected r^2 -scaled NIR scattered-light images, overplotted with synthetic arms, marked by dotted curve, with measured pitch angle of dominant spiral Fourier mode. (Right) Amplitude of Fourier spectra ($|A(m, p)|$), with arrow indicating the peak selected to calculate pitch angle. For DZ Cha, the peaks corresponding to the dominant open arm and the weaker, secondary tight arm (solid curve on the left) are labeled.

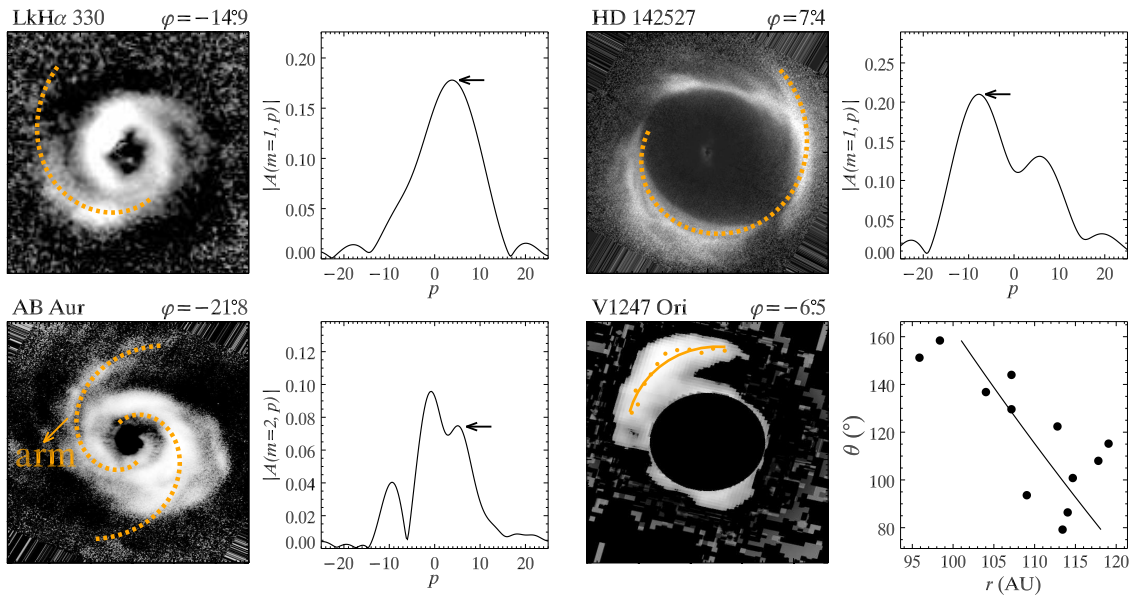


Figure 2. Same as in Figure 1, but for LkH α 330, HD 142527, and AB Aur. For V1247 Ori, the pitch angle is measured by identifying the local maxima (orange points in left panel; black points in right panel) along the arm, with an azimuthal step of 7° , and then fitting a logarithmic function to the spiral positions. The solid line marks the best-fit logarithmic function.

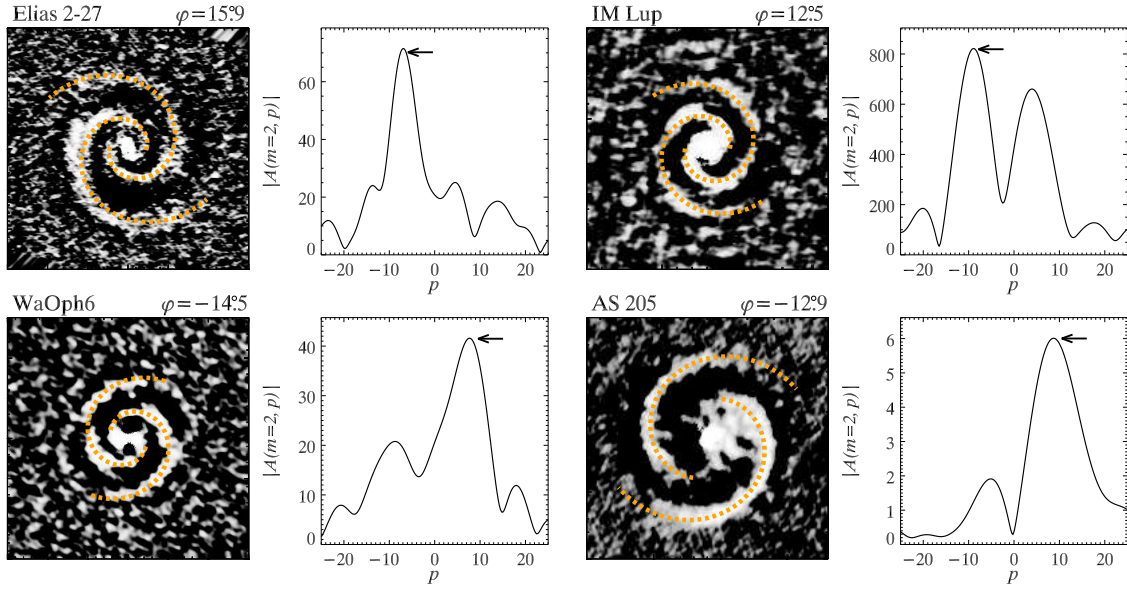


Figure 3. Same as in Figure 1, but for the residual non-axisymmetric component of deprojected ALMA millimeter images of Elias 2-27, IM Lup, WaOph 6, and AS 205N.

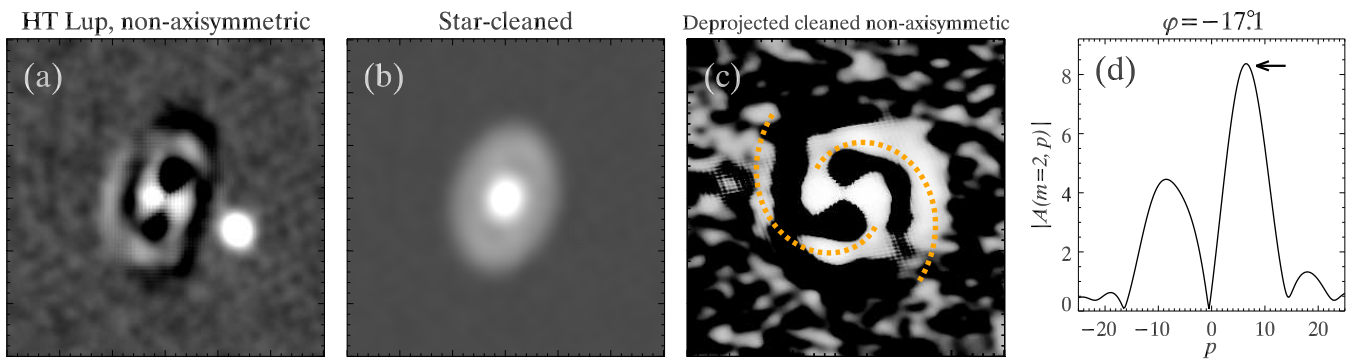


Figure 4. Spiral structure and pitch angle measurement for HT Lup: (a) residual non-axisymmetric component of ALMA millimeter image; (b) star-cleaned image; (c) residual non-axisymmetric component of deprojected star-cleaned image; (d) amplitude of Fourier spectra ($|A(m, p)|$) for residual deprojected star-cleaned image, with arrow indicating the peak selected to calculate pitch angle.

tion. The arms in the five ALMA millimeter continuum images are relatively fainter. To reduce the potentially adverse effect of radial variation of intensity, similar to the strategy in Huang et al. (2018), we construct the axisymmetric component of the disk by finding the median intensity within annuli of 1 AU width, with i and PA fixed to the values of the disk, and then subtract the axisymmetric component from the image to obtain the residual non-axisymmetric component for the pitch angle measurement.

We use i and PA to deproject the image from the previous step to its face-on orientation, employing the IRAF task `geotran`. As the ratio of scale height to radius varies from $\sim 10^{-2}$ near the star/disk interface to $\sim 10^{-1}$ near the outer edge of the disk (see Kenyon & Hartmann 1987; Dullemond et al. 2002), the disk is geometrically thin. Most of the disks in our sample are relatively face-on, with $i \lesssim 40^\circ$, mitigating projection effects.

Two-dimensional discrete Fourier transformation (2DDFT) is a well-defined and the most widely used technique to measure the pitch angle of spiral arms in disk galaxies (e.g., Kalnajs 1975; Iye et al. 1982; Krakow et al. 1982; Puerari & Dottori 1992; Puerari 1993; Block & Puerari 1999; Davis et al. 2012; Yu et al. 2018). The 2DDFT method decomposes images into Fourier components of different radial and azimuthal frequencies, i.e. spirals of different pitch angles and number of arms, and then chooses the dominant Fourier mode to calculate the pitch angle. In the context of galactic disks, this methodology has been useful in identifying physical relationships between spiral arm pitch angle and the global structure, mass, and kinematics of galaxies (Ma 2002; Seigar et al. 2005, 2006, 2008; Savchenko & Reshetnikov 2013; Kendall et al. 2015; Yu et al. 2018; Yu & Ho 2018, 2019). This work uses the 2DDFT method discussed in detail by Yu et al. (2018). Here, we just briefly summarize a few essential points. We transform the deprojected images into polar coordinates and decompose the light distribution into a superposition of 2D Fourier components

$$A(m, p) = \frac{1}{D} \int_{\ln(r_{\text{in}})}^{\ln(r_{\text{out}})} \int_{-\pi}^{\pi} \sum_{j=1}^N I_j(r_j, \theta_j) \delta(\mu - \mu_j) \delta(\theta - \theta_j) e^{-i(m\theta + p\mu)} d\theta d\mu, \quad (1)$$

with normalization factor $D = \sum_{j=1}^N I_j$, where I_j is the intensity of the j th pixel at (r_j, θ_j) , r_{in} and r_{out} the inner and outer boundary of the spiral structure, N the number of pixels within the radial range, and

$\mu \equiv \ln r$. The most prominent peak p_{max} of the power spectrum of spiral Fourier mode m is identified to calculate the pitch angle of the dominant spiral Fourier mode: $\varphi = \arctan\left(-\frac{m}{p_{\text{max}}}\right)$. As the 2DDFT method uses all pixel values within the imposed radial range to calculate the Fourier spectrum, the resulting pitch angle is an average value, with the flux as weighting, of different arms over the imposed radial range. In the event that any given arm is strong enough to dominate the Fourier spectrum, the resulting pitch angle will only trace such an arm. Following the strategy of Yu et al. (2018), the uncertainty of φ is estimated by repeating the measurement over three radial ranges: $[r_{\text{in}}, r_{\text{out}} - \Delta r]$, $[r_{\text{in}} + \Delta r, r_{\text{out}}]$, and $[r_{\text{in}} + \Delta r/2, r_{\text{out}} - \Delta r/2]$, where $\Delta r = (r_{\text{out}} - r_{\text{in}}) * 20\%$, to account for both the uncertainty of manually choosing the spiral arm boundary and the radial variation of pitch angle.

The 2D Fourier spectra ($|A(m, p)|$) and the synthetic arms with measured φ are presented in Figures 1–4. As shown in Figure 1, the spiral arms in the NIR scattered-light images of MWC 758, SAO 206462, DZ Cha, and HD 100453 clearly have two arms, and their Fourier spectra are dominated by the $m = 2$ mode. The prominent peak is selected to calculate φ . For MWC 758, we give a pitch angle of $19.2 \pm 1.0^\circ$. There are deviations between the observed spirals and the synthetic spirals, owing to the slight asymmetry of the two main arms and other short arms associated with the end of the right main arm. The 2DDFT method measures the average pitch angle for them. Our measured pitch angle is significantly larger than the result from Dong et al. (2015a; $\sim 11^\circ$), who determined the pitch angle by identifying the location of the spiral arms. Compared with their method, the 2DDFT technique has two major advantages. First, 2DDFT simultaneously considers all the fine spiral structures. Benisty et al. (2015) showed that, apart from the two main arms, the disk of MWC 758 has four additional non-axisymmetric features. Moreover, 2DDFT naturally weights by the intensity when calculating the Fourier components, making it sensitive to the structural information of the dominant spiral Fourier modes. This is also the reason why the measured pitch angle for DZ Cha, $\varphi = 26.6 \pm 3.1^\circ$, can only well trace the strong open arm, which dominates the Fourier spectrum with a single narrow peak. Multiple density waves may exist in DZ Cha. The dominant one is perhaps more closely associated with the formation physics of the global spiral structure. As discussed in Section 4, the pitch angle of the dominant component correlates strongly with the physical properties of the system. Nevertheless, the weaker arm, from visual inspection, should have a much smaller pitch angle, and

it is expected to contribute another peak to the left of the dominant peak. We thus use the secondary peak of the spectrum, as indicated in Figure 1, to calculate the pitch angle of the weaker arm, resulting in $10^\circ.3$. The mean pitch angle of the two arms of DZ Cha is 18° . The impact of DZ Cha on our results are discussed in Section 4. The measured pitch angle of SAO 206462 ($11^\circ.8 \pm 1^\circ.7$) is consistent with that reported in Dong et al. (2015a; $\sim 11^\circ$). The arms of HD 100453 are not perfectly symmetric, and the measured pitch angle, $\varphi = 15^\circ.4 \pm 0^\circ.7$, traces their average tightness.

Figure 2 presents the results for the sources without two clear arms in NIR scattered-light images. The Fourier spectrum of LkH α 330 is dominated by the $m = 1$ mode of the stronger of its two arms; the resulting pitch angle ($14^\circ.9 \pm 2^\circ.8$) is entirely consistent with the results of Uyama et al. (2018), who quoted $\sim 12^\circ$ for the strong arm and $\sim 16^\circ$ for the weaker one. For AB Aur, as the most prominent peak of the $m = 2$ Fourier mode has $p \approx 0$, the resulting “pitch angle” of $\sim 90^\circ$ corresponds to the central ring, which is not so symmetric in shape and light distribution. We use, instead, the secondary peak of the Fourier spectrum to calculate the pitch angle ($\varphi = 21^\circ.8 \pm 1^\circ.3$), whose synthetic arms well trace the main spiral arm indicated by the arrow in Figure 2. While AB Aur exhibits other arm pieces (Hashimoto et al. 2011) and small-scale gaseous arms inside the dust cavity (Tang et al. 2017), these short, faint arm pieces are likely a result of local instabilities and differential motion, stemming from formation physics very different from that of global spirals. The global disk properties are not expected to significantly affect such small-scale inner spirals. As we aim to systematically investigate the dependence of the global spiral pitch angle on disk properties, we do not consider the small-scale inner spirals. But, interestingly, the pitch angle of the inner western spirals ($\sim 20^\circ$) reported by Tang et al. (2017) is consistent with our measured pitch angle for the global spirals. HD 142527 has many small-scale feathery arms, but its Fourier spectrum is dominated by the $m = 1$ mode, which results in a tightly wound spiral of $\varphi = 7^\circ.4 \pm 0^\circ.5$. The 2DDFT method fails to measure the pitch angle for V1247 Ori, since its spiral arm is too tightly wound and too short in radial extent. We measure its pitch angle by identifying a number of local maxima within the arm, in azimuthal steps of 7° . Then the pitch angle is estimated by fitting a logarithmic function to the positions of the local maxima in the arm.

Figures 3–4 plot the pitch angle measurements for the five ALMA continuum images. Elias 2-27, IM Lup, WaOph 6, and AS 205 have two symmetric arms with

Fourier spectra dominated by an $m = 2$ mode. We find pitch angle $\varphi = 15^\circ.9 \pm 2^\circ.4$ for Elias 2-27, $\varphi = 14^\circ.5 \pm 3^\circ.1$ for WaOph 6, and $\varphi = 12^\circ.9 \pm 1^\circ.1$ for AS 205; these values are consistent with those reported in Huang et al. (2018) and Kurtovic et al. (2018). We assign a global pitch angle $\varphi = 12^\circ.5 \pm 2^\circ.7$ to IM Lup; the pitch angle of the spiral arms in this object decreases from $\sim 19^\circ$ in the inner region to $\sim 10^\circ$ in the outer part (Huang et al. 2018).

As shown in Figure 4a, the spiral arms in the non-axisymmetric component of HT Lup are not symmetric. In particular, the clear spiral arm to the east was not identified by Kurtovic et al. (2018) for measuring pitch angle, whereas the corresponding arm to the west is nearly invisible. Note that there is a strong central bar in this system. A close stellar companion to the southwest may potentially contaminate the Fourier spectra. We removed the star by fitting a Gaussian function to it in the residual non-axisymmetric component image, and then subtracting it from the original image to construct the star-cleaned image (Figure 4b). We then generate a residual star-cleaned non-axisymmetric component image and deproject it (Figure 4c) for Fourier decomposition. The Fourier spectrum (Figure 4d) presents a prominent peak, which yields $\varphi = 17^\circ.1 \pm 0^\circ.8$. Our measured pitch angle is significantly larger than that in Kurtovic et al. (2018), probably due to their omission of the eastern arm and the arm intensity varying significantly with radius.

4. RESULTS AND DISCUSSION

4.1. Dependence of Pitch Angle on Disk Size, Luminosity, and Mass

Figure 5 plots the measured pitch angles of dominant spiral Fourier mode against the central star mass, disk radius, disk aspect ratio, and disk mass. The open and solid symbols mark, respectively, the results for NIR scattered-light images and ALMA millimeter images, and the blue symbols denote the four systems (HD 142527, HD 100453, AS 205, and HT Lup) with a known companion. The measured pitch angles hardly correlate with the mass of the central star (Figure 5a; Pearson correlation coefficient $\rho = -0.14$), but there is a weak tendency for more tightly wound arms to reside in disks with somewhat larger sizes (Figure 5b; $\rho = -0.42$) and higher aspect ratios (Figure 5c; $\rho = -0.34$). Most strikingly, we found a strong inverse correlation between pitch angle and disk mass: smaller pitch angles are associated with more massive protoplanetary disks (Figure 5e; $\rho = -0.81$). Fitting a logarithmic function gives

$$|\varphi| = -(7.8 \pm 1.7) \log(M_D/M_\odot) + (2.7 \pm 2.6), \quad (2)$$

Table 1. Spiral Arm Pitch Angles and Properties of Protoplanetary Disks and their Central Stars

Object	i	PA	R_D	M_*	$f_{880\mu\text{m}}$	M_D	L_*	Q	H/R	$ \varphi $	References
	(deg)	(deg)	(AU)	(M_\odot)	(mJy)	($0.01 M_\odot$)	(L_\odot)			(deg)	
(1)	(2)	(3)	(4)	(5)	(6)	(7)	(8)	(9)	(10)	(11)	(12)
MWC 758	21	65	151	1.68	180	1.18	8.5	11	0.08	19.2 ± 1.0	1,2,3,2,3,2
SAO 206462	11.5	64	156	1.70	620	4.08	8.8	3	0.08	11.0 ± 1.0	4, 2,3,2,3,5
LkH α 330	31	91	170	2.12	210	3.39	12.8	5	0.08	14.9 ± 2.8	6,2,3,2,3,7
DZ Cha	43	176	22	0.51	21	0.20	0.6	16	0.06	26.6 ± 3.1	8, ..., 3,8,3,8
AB Aur	36.6	26.8	230	2.50	317	1.50	43.8	14	0.09	21.8 ± 1.3	9,10,3,11,3,11
HD 142527	20	299	300	1.70	3310	33.8	9.9	0.5	0.10	7.4 ± 0.5	12,13,3,13,3,5
V1247 Ori	31.3	104	190	1.91	292	7.64	15.8	2	0.09	6.5 ± 0.7	14,15,3,15,3,5
HD 100453	38	142	48	1.53	464	1.74	6	5	0.06	15.4 ± 0.7	16,16,3,17,3,5
Elias 2-27	56.2	118.8	300	0.5	666	10.4	1.0	0.6	0.13	15.9 ± 2.4	18,19,20, ..., ..., 21
IM Lup	47.5	144.5	300	0.6	582	18.4	0.9	0.4	0.12	12.5 ± 2.7	18,22,3,22,3,22
WaOph 6	47.3	174.2	137	0.7	386	2.17	2.9	3	0.10	14.5 ± 2.3	18, ..., 20, ..., ..., 21
AS 205	20.1	114.0	60	0.9	872	3.28	2.1	2	0.07	12.9 ± 1.1	23, ..., 20, ..., ..., 24
HT Lup	48.1	166.1	37	1.7	175	0.53	5.5	17	0.05	17.1 ± 0.8	23, ..., 20, ..., ..., 25

NOTE— Col. (1): Source name. Col. (2): Inclination angle. Col. (3): Position angle; references same as in Col. (2). Col. (4): Radius of the disk in millimeter continuum emission, except for DZ Cha, whose disk radius is estimated using NIR scattered-light images from Canovas et al. (2018); disk radius of WaOph 6, AS 205, and HT Lup are determined in this work using ALMA millimeter images. Col. (5): Mass of central star. Col. (6): Flux density at $880 \mu\text{m}$ ($f_{880\mu\text{m}}$); $f_{880\mu\text{m}}$ of Elias 2-27, WaOph 6, AS 205, and HT Lup are obtained by interpolation of SED collected by Andrews et al. (2018); others are determined by converting the flux densities given in the reference listed in Col. (12) to flux densities at $880 \mu\text{m}$ through a power law $f_\nu \propto \nu^{2.4}$. Col. (7): Disk mass; disk masses of Elias 2-27, WaOph 6, AS 205, and HT Lup are derived in this work following the procedure in Dong et al. (2018b). Col. (8): Luminosity of central star. Col. (9): Mean Toomre’s Q of the disk. Col. (10): Disk aspect ratio at $r = R_D$. Col. (11): Measured pitch angle of spiral arms. Col. (12): Literature references for i , R_D , M_* , the flux densities used to calculate $f_{880\mu\text{m}}$, M_D , and L_* : (1) Benisty et al. (2015), (2) Andrews et al. (2011), (3) Dong et al. (2018a), (4) Muto et al. (2012), (5) Fairlamb et al. (2015), (6) Uyama et al. (2018), (7) van der Marel et al. (2016), (8) Canovas et al. (2018), (9) Hashimoto et al. (2011), (10) Tang et al. (2012), (11) Andrews et al. (2013), (12) Pontoppidan et al. (2011), (13) Boehler et al. (2017), (14) Ohta et al. (2016), (15) Kraus et al. (2017), (16) Benisty et al. (2017), (17) van der Plas et al. (2019), (18) Huang et al. (2018), (19) Pérez et al. (2016), (20) Andrews et al. (2018), (21) Andrews et al. (2009), (22) Cleeves et al. (2016), (23) Kurtovic et al. (2018), (24) Barenfeld et al. (2016), (25) Alcalá et al. (2017).

with a scatter of 3° in pitch angle or 0.4 dex in disk mass. Since more massive disks tend to be larger, the weak $\varphi - R_D$ relation is likely a secondary manifestation of the stronger primary $\varphi - M_D$ relation. Systems with known companions also follow the same empirical trend. If we only consider the results from the ALMA millimeter images, the correlation between pitch angle and disk mass becomes shallower, but this may be an artifact of the narrow range of pitch angles ($12^\circ - 17^\circ$) probed by this subset of points. The largest source of uncertainty in Equation (2) lies in the disk masses. Although all the masses were derived using a uniform method (Dong et al. 2018b), systematic biases may exist. In particular, the gas-to-dust mass ratio adopted in this method has not been well-constrained. The estimated disk mass may not be the true mass, but it can be related to other physical quantities of the disk (e.g. tempera-

ture, size, and dust mass). Other methods of estimating disk mass based on gas tracers (CO or HD) report significantly different results (e.g., Bergin & Williams 2017). There may be a systematic offset between the absolute disk masses derived from dust emission compared to those derived from other tracers. While such a systematic offset will quantitatively change the form of the $\varphi - M_D$, the qualitative nature of the physical dependence between pitch angle and disk mass should still be preserved. With these caveats in mind, Figure 5e suggests that, independent of the formation mechanism, the disk mass plays a fundamental role in determining the pitch angle of the observed spiral structure.

In light of the significant uncertainties associated with the disk masses, we verify that pitch angle correlates nearly equally well with the model-independent submillimeter flux density (Figure 5d; $\rho = -0.76$), such that

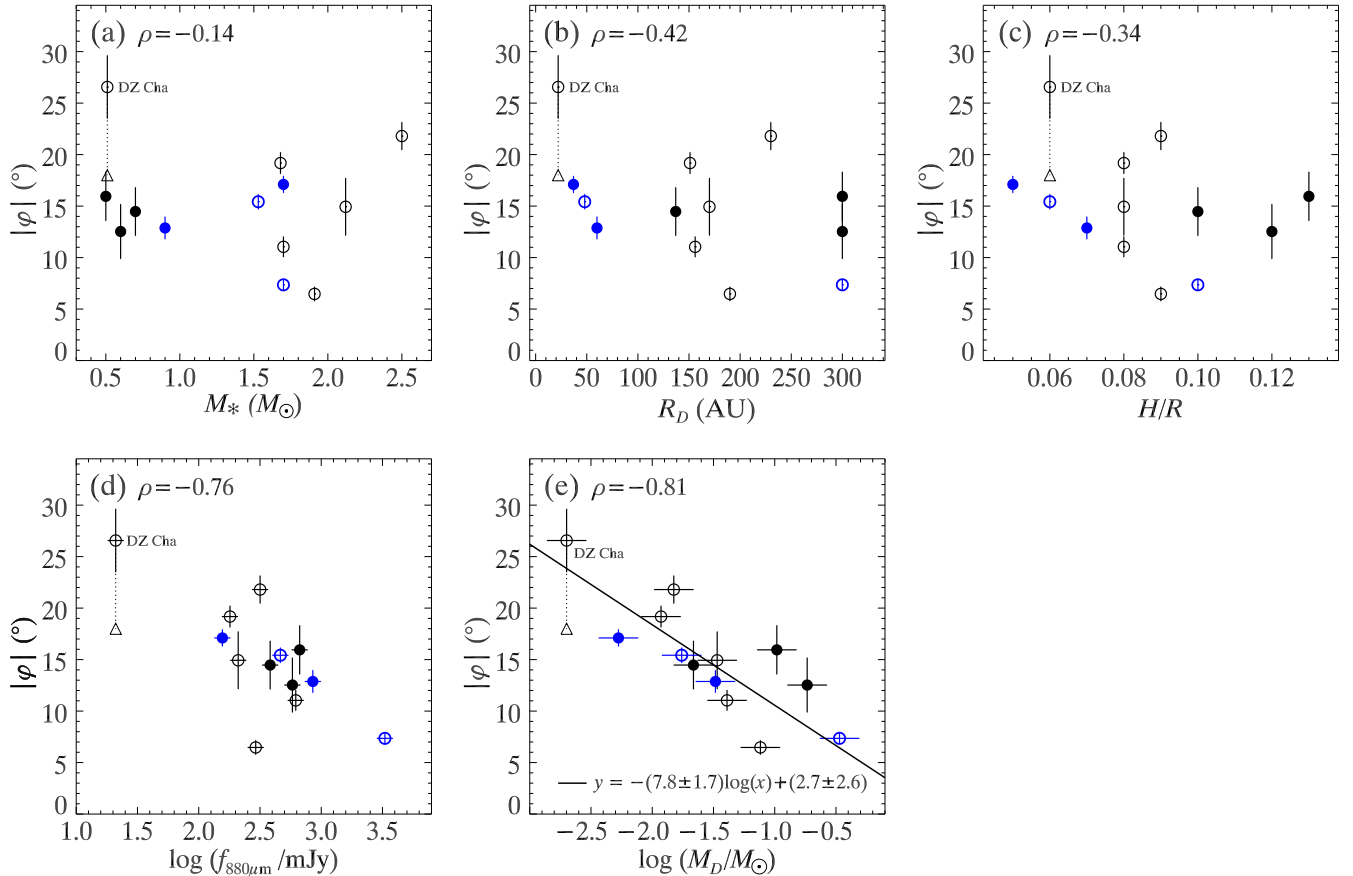


Figure 5. Relationship between pitch angle of dominant spiral Fourier mode (φ) and (a) mass of central star (M_*), (b) disk radius (R_D), (c) disk aspect ratio (H/R), (d) flux density at $880\mu\text{m}$ ($f_{880\mu\text{m}}$), and (e) disk mass (M_D). The open and solid symbols mark the results for NIR scattered-light images and ALMA millimeter images, respectively. The blue symbols denote objects with a known companion. The best-fit function (solid line) in (d) has the form given in the bottom of the panel. The Pearson correlation coefficient (ρ) is shown in the top of each panel. The mean pitch angle of the dominant open arm and the weaker tight arm (18° ; triangle) of DZ Cha are especially marked.

disks with brighter submillimeter flux density tend to have more tightly wound spiral arms.

DZ Cha deserves special comment. The pitch angle derived from the dominant spiral Fourier mode well traces the stronger arm but not the weaker one, and its high value ($\varphi = 26.6 \pm 3.1$) has a strong effect on the empirical trends in Figure 5. If we exclude DZ Cha, the $\varphi - R_D$ and $\varphi - H/R$ relations become much weaker, with ρ reducing to -0.22 and -0.18 , respectively. But without DZ Cha the $\varphi - f_{880\mu\text{m}}$ ($\rho = -0.56$) and $\varphi - M_D$ ($\rho = -0.70$) relations remain strong. Under the possibility that the mean pitch angle of the two arms of DZ Cha is more fundamental, setting the pitch angle to 18° (triangle in Figure 5) reduces the Pearson’s correlation coefficient of the $\varphi - f_{880\mu\text{m}}$ and $\varphi - M_D$ relations to -0.55 and -0.69 , respectively, but still preserves their statistical significance. Therefore, DZ Cha weakens but does not strongly affect the main conclusions of this study.

4.2. Discussion

Traditional numerical simulations of isolated protoplanetary disks can generate transient but recurrent material spiral arms (e.g., Lodato & Rice 2004; Rice et al. 2004; Forgan et al. 2011), but, contrary to observations, they generally produce significantly more than two arms. Although recent simulations show that two material arms can also arise (Dong et al. 2015b; Tomida et al. 2017), their short life times, if owing to gravitational instability, implies that they are statistically less likely to be observed. The frequent change of shape of these material spiral arms makes it difficult to maintain pitch angles long-lived enough to produce the observed strong $\varphi - M_D$ relation.

Shadowing from a misaligned inner disk can trigger spiral arms detected in scattered light (Montesinos et al. 2016; Montesinos & Cuello 2018). Although a less massive disk may be associated with more open arms at

the onset their formation, the arms become tighter with time and eventually evolve into tight arms with $\varphi \approx 13^\circ$ (Montesinos et al. 2016). Besides, the five disks observed in millimeter continuum used in this work do not reveal evidence of a misaligned inner disk (also see Huang et al. 2018). In particular, there are no signatures of shadowing in IM Lup in scattered light (Avenhaus et al. 2018).

Studying spiral wakes in a non-gravitating disk excited by a planet, Rafikov (2002) showed that the spiral arm pitch angle depends on the temperature of the disk and the location of the planet. Pursuing this further, Zhu et al. (2015) carried out three-dimensional hydrodynamical simulations and found that, as a consequence of the non-linear evolution of the spiral wave propagation, planet-excited spirals have a larger pitch angle with a more massive perturber. In this scenario, the pitch angle depends on the location and mass of the perturbing plane, not explicitly on the surface density and/or mass of the disk. Thus, this scenario is unlikely to explain our results.

Another possible mechanism may be density wave theory (Lin & Shu 1964; Bertin & Lin 1996). In a massive thin disk, tightly wound spirals, formed via internal gravitational instability, would have maximum growth rate at wavenumber $k = \pi G \Sigma / c_s^2$, resulting in pitch angle

$$\varphi \propto \frac{c_s^2}{\Sigma r}, \quad (3)$$

where c_s , Σ , and r are the sound speed, mass surface density, and radial distance (Hozumi 2003). Adopting a simple power-law distribution $\Sigma \propto \Sigma_0 r^{-p}$, where $\Sigma_0 \propto M_D / R_D^2$, and $c_s^2 \propto T \propto L_*^{0.25} r^{-q}$, we have

$$\varphi \propto \frac{L_*^{0.25}}{M_D} R_D^2 r^{p-q-1}. \quad (4)$$

The criterion $Q < 1$ for an unstable disk is derived for local axisymmetric Jeans instabilities, but for non-axisymmetric disturbances the threshold value of Q is marginally larger than 1. Thus, Eq. (4) is valid for a massive disk with Toomre's Q less than or slightly larger than 1 (Table 1). This may explain the trend that pitch angle decreases with larger mass for massive disks, namely the high-mass end of the $\varphi - M_D$ relation. However, light disks are characterized by Toomre's $Q \gg 1$. Equation (4) does not apply to them. Light disks are stable against gravitational instability, and an external disturber may be to trigger spiral structure.

Even though Eq. (3) is valid only for a massive disk, it may still shed light on understanding spirals in a light disk. Eq. (3) implies that spirals would be more open

(larger $|\varphi|$) if the material responding to the perturbation is hotter (higher c_s). In other words, spirals observed in NIR scattered-light images may be more open than their counterparts observed in dust millimeter continuum emission. On the other hand, the 3-D structure of spirals can be more complicated than this simple argument. Juhász & Rosotti (2018) found that the spirals at the disk atmosphere, which is several times hotter than the disk midplane, are only slightly more open than the spirals at the disk midplane. MWC 758 was observed in both bands. As the arms of MWC 758 are much less symmetric and regular in the dust continuum than in the NIR, we did not attempt to analyze its millimeter image. However, Dong et al. (2018a) show that the spiral arms of MWC 758 in millimeter continuum indeed are slightly tighter than in NIR scattered light, consistent with our expectations.

5. SUMMARY

We use two-dimensional Fourier transformation to measure the pitch angle of the dominant spiral Fourier mode for 13 protoplanetary disks imaged in the NIR in scattered light and in millimeter dust continuum emission. The measured pitch angles correlate well with 880 micron flux density, such that disks with brighter submillimeter flux densities tend to have more tightly wound spiral arms. Most strikingly, the pitch angle exhibits a strong inverse correlation with the disk mass, following $|\varphi| = -(7.8 \pm 1.7) \log(M_D / M_\odot) + (2.7 \pm 2.6)$. Four disks with a known companion also obey this scaling relation. Such a strong dependence of pitch angle on disk mass is not expected in the theory or hydrodynamical simulations of non-gravitating disks. In contrast, density wave theory may partly explain the $\varphi - M_D$ relation in the high-mass end. Our result suggests that disk mass, independent of the formation mechanism, plays a fundamental role in determining the pitch angle of the observed spiral arms. The empirical correlation revealed in this work provides a simple empirical, independent method to use the pitch angle of spiral arms to constrain the mass of protoplanetary disks.

SY and LH acknowledge support from the National Science Foundation of China (11721303) and the National Key R&D Program of China (2016YFA0400702). ZZ acknowledges support from the National Science Foundation under CAREER Grant Number AST-1753168 and the Sloan Foundation. We thank the very constructive suggestions from the referee. We thank Ruobing Dong, Gregory Herczeg, and Feng Long for helpful discussions and valuable advice. We are grateful to Henning Avenhaus, Myriam Benisty, Hector Canovas,

Antonio Garufi, and Jun Hashimoto for making available the observational images used in Figures 1 and 2. This paper makes use of the following ALMA data: ADS/JAO.ALMA#2016.1.00484.L. ALMA is a partnership of ESO (representing its member states),

NSF (USA), and NINS (Japan), together with NRC (Canada), NSC and ASIAA (Taiwan), and KASI (Republic of Korea), in cooperation with the Republic of Chile. The Joint ALMA Observatory is operated by ESO, AUI/NRAO, and NAOJ.

REFERENCES

- Adams, F. C., Ruden, S. P., & Shu, F. H. 1989, *ApJ*, 347, 959
- Alcalá, J. M., Manara, C. F., Natta, A., et al. 2017, *A&A*, 600, A20
- Andrews, S. M., Huang, J., Pérez, L. M., et al. 2018, *ApJL*, 869, L41
- Andrews, S. M., Rosenfeld, K. A., Kraus, A. L., & Wilner, D. J. 2013, *ApJ*, 771, 129
- Andrews, S. M., Wilner, D. J., Espaillat, C., et al. 2011, *ApJ*, 732, 42
- Andrews, S. M., Wilner, D. J., Hughes, A. M., Qi, C., & Dullemond, C. P. 2009, *ApJ*, 700, 1502
- Avenhaus, H., Quanz, S. P., Garufi, A., et al. 2018, *ApJ*, 863, 44
- Avenhaus, H., Quanz, S. P., Schmid, H. M., et al. 2017, *AJ*, 154, 33
- Bae, J., & Zhu, Z. 2018, *ApJ*, 859, 118
- Barenfeld, S. A., Carpenter, J. M., Ricci, L., & Isella, A. 2016, *ApJ*, 827, 142
- Benisty, M., Juhasz, A., Boccaletti, A., et al. 2015, *A&A*, 578, L6
- Benisty, M., Stolker, T., Pohl, A., et al. 2017, *A&A*, 597, A42
- Bergin, E. A., & Williams, J. P. 2017, *ASSL*, 445, 1
- Bertin, G., & Lin, C. C. 1996, *Spiral Structure in Galaxies a Density Wave Theory* (Cambridge, MA: MIT Press)
- Block, D. L., & Puerari, I. 1999, *A&A*, 342, 627
- Boehler, Y., Ricci, L., Weaver, E., et al. 2018, *ApJ*, 853, 162
- Boehler, Y., Weaver, E., Isella, A., et al. 2017, *ApJ*, 840, 60
- Canovas, H., Montesinos, B., Schreiber, M. R., et al. 2018, *A&A*, 610, A13
- Cleeves, L. I., Öberg, K. I., Wilner, D. J., et al. 2016, *ApJ*, 832, 110
- Davis, B. L., Berrier, J. C., Shields, D. W., et al. 2012, *ApJS*, 199, 33
- Dong, R., Hall, C., Rice, K., & Chiang, E. 2015, *ApJL*, 812, L32
- Dong, R., Liu, S.-Y., Eisner, J., et al. 2018, *ApJ*, 860, 124
- Dong, R., Najita, J. R., & Brittain, S. 2018, *ApJ*, 862, 103
- Dong, R., Zhu, Z., Fung, J., et al. 2016, *ApJL*, 816, L12
- Dong, R., Zhu, Z., Rafikov, R. R., & Stone, J. M. 2015, *ApJL*, 809, L5
- Dullemond, C. P., van Zadelhoff, G. J., & Natta, A. 2002, *A&A*, 389, 464
- Fairlamb, J. R., Oudmaijer, R. D., Mendigutía, I., Ilee, J. D., & van den Ancker, M. E. 2015, *MNRAS*, 453, 976
- Follette, K. B., Rameau, J., Dong, R., et al. 2017, *AJ*, 153, 264
- Forgan, D., Rice, K., Cossins, P., & Lodato, G. 2011, *MNRAS*, 410, 994
- Garufi, A., Benisty, M., Pinilla, P., et al. 2018, *A&A*, 620, A94
- Garufi, A., Quanz, S. P., Avenhaus, H., et al. 2013, *A&A*, 560, A105
- Grady, C. A., Muto, T., Hashimoto, J., et al. 2013, *ApJ*, 762, 48
- Hashimoto, J., Tamura, M., Muto, T., et al. 2011, *ApJL*, 729, L17
- Hozumi, S. 2003, in *Lecture Notes in Physics*, Vol. 626: *Galaxies and Chaos*, ed. G. Contopoulos & N. Voglis (Berlin: Springer), 380
- Huang, J., Andrews, S. M., Pérez, L. M., et al. 2018, *ApJL*, 869, L43
- Iye, M., Okamura, S., Hamabe, M., & Watanabe, M. 1982, *ApJ*, 256, 103
- Juhász, A., & Rosotti, G. P. 2018, *MNRAS*, 474, L32
- Kalnajns, A. J. 1975, *La Dynamique des Galaxies Spirales*, 241, 103
- Kendall, S., Clarke, C., & Kennicutt, R. C. 2015, *MNRAS*, 446, 4155
- Kenyon, S. J., & Hartmann, L. 1987, *ApJ*, 323, 714
- Kley, W., & Nelson, R. P. 2012, *ARA&A*, 50, 211
- Krakow, W., Huntley, J. M., & Seiden, P. E. 1982, *AJ*, 87, 203
- Kraus, S., Kreplin, A., Fukugawa, M., et al. 2017, *ApJL*, 848, L11
- Kurtovic, N., Pérez, L., Benisty, M., et al. 2018, *ApJL*, 869, L44
- Laughlin, G., & Rozyczka, M. 1996, *ApJ*, 456, 279
- Lin, C. C., & Shu, F. H. 1964, *ApJ*, 140, 646
- Lodato, G., & Rice, W. K. M. 2004, *MNRAS*, 351, 630
- Ma, J. 2002, *A&A*, 388, 389
- Meru, F., Juhász, A., Ilee, J. D., et al. 2017, *ApJL*, 839, L24
- Miranda, R., & Rafikov, R. R. 2019, *ApJ*, 875, 37

- Montesinos, M., & Cuello, N. 2018, MNRAS, 475, L35
- Montesinos, M., Perez, S., Casassus, S., et al. 2016, ApJL, 823, L8
- Muto, T., Grady, C. A., Hashimoto, J., et al. 2012, ApJL, 748, L22
- Noh, H., Vishniac, E. T., & Cochran, W. D. 1991, ApJ, 383, 372
- Ohta, Y., Fukagawa, M., Sitko, M. L., et al. 2016, PASJ, 68, 53
- Pérez, L. M., Carpenter, J. M., Andrews, S. M., et al. 2016, Science, 353, 1519
- Pontoppidan, K. M., Blake, G. A., & Smette, A. 2011, ApJ, 733, 84
- Puerari, I. 1993, PASP, 105, 1290
- Puerari, I., & Dottori, H. A. 1992, A&AS, 93, 469
- Rafikov, R. R. 2002, ApJ, 569, 997
- Rice, W. K. M., Lodato, G., Pringle, J. E., Armitage, P. J., & Bonnell, I. A. 2004, MNRAS, 355, 543
- Savchenko, S. S., & Reshetnikov, V. P. 2013, MNRAS, 436, 1074
- Seigar, M. S., Block, D. L., Puerari, I., Chorney, N. E., & James, P. A. 2005, MNRAS, 359, 1065
- Seigar, M. S., Bullock, J. S., Barth, A. J., & Ho, L. C. 2006, ApJ, 645, 1012
- Seigar, M. S., Kenefick, D., Kenefick, J., & Lacy, C. H. S. 2008, ApJL, 678, L93
- Shu, F. H., Tremaine, S., Adams, F. C., & Ruden, S. P. 1990, ApJ, 358, 495
- Skrutskie, M. F., Dutkevitch, D., Strom, S. E., et al. 1990, AJ, 99, 1187
- Strom, K. M., Strom, S. E., Edwards, S., Cabrit, S., & Skrutskie, M. F. 1989, AJ, 97, 1451
- Tang, Y.-W., Guilloteau, S., Dutrey, A., et al. 2017, ApJ, 840, 32
- Tang, Y.-W., Guilloteau, S., Piétu, V., et al. 2012, A&A, 547, A84
- Tomida, K., Machida, M. N., Hosokawa, T., Sakurai, Y., & Lin, C. H. 2017, ApJL, 835, L11
- Uyama, T., Hashimoto, J., Muto, T., et al. 2018, AJ, 156, 63
- van der Marel, N., Verhaar, B. W., van Terwisga, S., et al. 2016, A&A, 592, A126
- van der Plas, G., Ménard, F., Gonzalez, J.-F., et al. 2019, A&A, 624, A33
- Wagner, K., Apai, D., Kasper, M., & Robberto, M. 2015, ApJL, 813, L2
- Yu, S.-Y., & Ho, L. C. 2018, ApJ, 869, 29
- Yu, S.-Y., & Ho, L. C. 2019, ApJ, 871, 194
- Yu, S.-Y., Ho, L. C., Barth, A. J., & Li, Z.-Y. 2018, ApJ, 862, 13
- Zhu, Z., Dong, R., Stone, J. M., & Rafikov, R. R. 2015, ApJ, 813, 88